

Performance of a longitudinally-segmented CsI(Tl) array suitable for a detector in a low or medium energy e^+e^- storage ring*

R. Baggs,^a E. Church,^b V. Cook,^b D. Coward,^a R. Coxe,^a K. Curtis,^c
R. S. Davis,^d J. Dyke,^c A. Foland,^e R. Frey,^f D. Freytag,^a G. Gladding,^e
J. M. Izen,^d R. A. Johnson,^c M. E. King,^a W. Lockman,^g G. Niemi,^a
G. Putallaz,^a R. H. Schindler,^a D. P. Stoker,^h F. Toevs,^b E. Vokurka,^{a,e}
E. Weiss^b

^aStanford Linear Accelerator Center, Stanford, CA 94309

^bUniversity of Washington, Seattle, WA 98195

^cUniversity of Cincinnati, Cincinnati, OH 45221

^dUniversity of Texas, Dallas, TX 75083

^eUniversity of Illinois, Champaign-Urbana, IL 61801

^fUniversity of Oregon, Eugene, OR 97403

^gUniversity of California, Santa Cruz, CA 95064

^hUniversity of California, Irvine, CA 92717

We present results on energy resolution and linearity, and position resolution, from a test of an array of CsI(Tl) crystals in a $\pi/e/\mu$ beam (120 to 400 MeV) at TRIUMF. The crystal array was designed to study the effects of longitudinal and transverse crystal segmentation on energy and position resolution and background rejection. We also studied the feasibility of a wavelength-shifter and multi-photodiode readout system, suitable for use in magnetic detectors at low and medium energy, high-luminosity e^+e^- storage rings. Energy resolutions of $(1.69 \pm 0.08)\%/\sqrt{E(\text{GeV})}$ and $(1.83 \pm 0.05)\%/\sqrt{E(\text{GeV})}$ were obtained for two different crystal tower configurations. Position resolution of 6.5 (9.0) mm was obtained at 300 (120) MeV for a 2×2 square array of four $4 \times 4 \times 7.4 \text{ cm}^3$ crystals transverse to the beam.

Submitted to *Nuclear Instruments & Methods in Physics Research - A*

* Work supported in part by Department of Energy Contract DE-AC03-76SF00515, DE-FG03-91ER40679, and DE-FG05-92ER40736.

1. Introduction

Several high-luminosity, low and medium-energy e^+e^- storage rings are presently being built or are under consideration for future construction; *e.g.*, the so-called Phi, Tau-Charm, and B-Factories. Each of these facilities will require a state-of-the-art detector with high precision electromagnetic calorimetry. Numerous studies [1] of requirements for these detectors suggest that many characteristics of CsI crystal calorimetry are necessary to achieve their physics goals. Notably, the high light yield ($\sim 50,000$ photons/MeV) of CsI(Tl) or CsI(Na) facilitates excellent energy resolution and efficient detection of photons with energies down to a few MeV. Excellent position and angular resolution is also obtainable at these energies. The large light output makes feasible the use of low-gain or unity-gain devices, such as photodiodes, for readout. The dominant drawbacks of CsI scintillators are low radiation hardness, poor mechanical properties, and relatively long decay times ($\sim 1 \mu s$ for Tl-doped crystals) which integrate scintillation light over many beam crossings. This results in serious sources of low-energy "fake" photons from the pileup of backgrounds from lost beam particles, nuclear interactions of hadrons, and albedo within an event. While radiation hardness is not an issue at Phi and Tau-Charm Factories [2], evidence from experiments with large CsI arrays suggests that albedo and pileup may limit the use of the lowest energy photons (≤ 20 MeV) if these backgrounds are not adequately suppressed. Hence, these crystals should not be considered for such future colliders unless these problems are addressed [3]. We present herein results of detailed studies of an array of CsI(Tl) crystals designed to overcome some of these limitations by use of alternative crystal geometries, crystal segmentation, and photodiode/wavelength-shifting plastic readout techniques.

2. Calorimeter and Test Design

We tested an array of 14 CsI(Tl) crystal towers which could be scaled to a full-sized cylindrical detector suitable for use at low and medium energy "factories". Physics and cost considerations imply that such a CsI calorimeter would typically contain about 10,000 projective towers in a cylinder ~ 3.5 meters long with ~ 1 meter inner radius, for a total of 8-10 m^3 of crystals. The towers would be of transverse size (40-80 mr) \times (40-80 mr), and 16-18 radiation lengths (rl) (29.6-33.3 cm) long, tapered along their major axis to form truncated pyramids. To enhance $\pi/e/\mu$ separation and improve the rejection of fake photons, each tower can be segmented longitudinally into two or more parts. Depending on the average energy in the collisions, a break near shower

maximum, at ~ 3 to 4 rl (5.6-7.4 cm), would be chosen. To improve position resolution, the short, front section can also be divided transversely.

The electronics for the calorimeter has strict limits on inherent noise, as discussed in Section 2.6 and Section 3.3. It is desirable to locate close to the source most of the signal processing, such as amplification, pulse shaping, calibration, and drivers. Since these electronics would be inaccessible during an experimental run, a high degree of reliability is needed. Spatial constraints and heat dissipation are also considerations in the design. Semi-custom arrays of bipolar transistors, which are compact, and have reliable interconnections, and have low heat dissipation due to low internal capacitive loads, are effective in this environment. The electronics used in this beam test was a first approach to a system realized in semi-custom bipolar transistor technology. To allow energy to be unambiguously associated with a beam crossing, we also anticipate a need to incorporate coarse timing information into the readout of a final device; however, this was not addressed by our test.

2.1 *TRIUMF Beamline and Instrumentation*

The test of a longitudinally-segmented CsI(Tl) array was conducted in the TRIUMF M11 and M13 beamlines. In this paper, only results from data taken in the higher momentum M11 beamline are presented. A schematic of part of the beamline is shown in Fig. 1. Initially, protons with energy up to 520 MeV from the TRIUMF cyclotron incident upon a 1 cm-thick carbon target produce pions. Pion decay to muons, and muon decay to electrons, produce a final beam containing electrons, pions, and muons. Beams of momentum up to 416 MeV/c are transported through two 60° -bend dipole magnets (B1 and B2) and a series of quadrupole magnets to a doubly achromatic beam spot at the experimental focus. The momentum scale of the M11 beamline is known from the B1 magnetic field strength to $\pm 0.25\%$ [4]. Readout of data was triggered by a coincidence of RF timing from the TRIUMF cyclotron with signals in two 3 mm-thick scintillators, S1 and S2. To avoid pileup, upstream collimators were used to reduce the rate of incident particles to ~ 100 Hz. Signals from the S2 scintillator and RF were used to measure time-of-flight (TOF), which provided modest π/e separation up to ~ 400 MeV. A low-mass, eight-wire drift chamber was used to measure the vertical and horizontal positions and angle of the beam at the crystal face. Fourteen crystal towers were stacked in a light-tight aluminum box through which dry N_2 flowed. The dry box contained a thin aluminum foil beam entrance window.

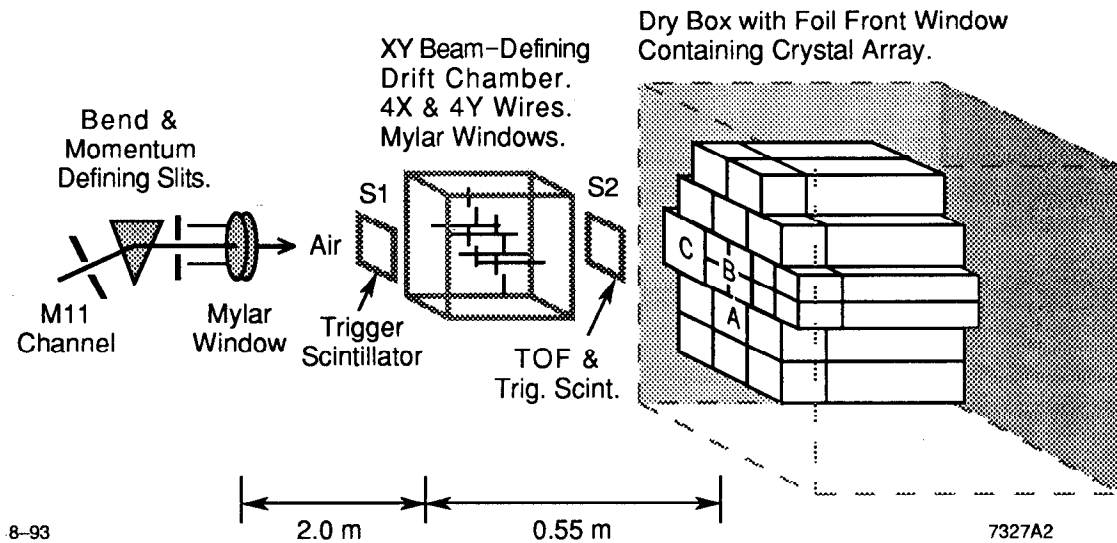


Fig. 1. A portion of the TRIUMF M11 beamline with trigger scintillators S1 and S2, beam-defining drift chamber, and CsI crystal tower array in dry box. The locations of Towers A, B, and C discussed in the text are indicated.

2.2 Geometry of Crystal Array

CsI(Tl) crystals for the test were procured from four manufacturers: Horiba Crystal Products, Quartz and Silice, Bicron Corp., and Crystran Merck Ltd. The thallium doping level varied by manufacturer but was typically around 1000 ppm. Each tower contained a 16 rl CsI crystal, subdivided into a front section (4 rl) and a back section (12 rl). Three lateral geometries were considered: crystals of rectangular cross section with faces of $6.4 \times 6.4 \text{ cm}^2$, front and back, and an $8.0 \times 8.0 \text{ cm}^2$ face in the back, either subdivided four-fold in the front, or not, as shown in Fig. 2. While the four-fold segmentation in the front tower may give better position resolution and provide pattern recognition capability to improve background rejection, the additional surfaces, edges, and readout photodiodes could result in poorer overall performance. Addressing these issues is the basis of this study.

The beam test array consisted of 11 $6.4 \times 6.4 \text{ cm}^2$ and three $8.0 \times 8.0 \text{ cm}^2$ crystal towers. Two of the $8.0 \times 8.0 \text{ cm}^2$ towers (e.g., Tower B in Fig. 2) were segmented four-fold in front, as described above. Each crystal within a tower was optically separated from the other crystals with a wrapping of three layers of PTE Teflon (0.08 mm total thickness) and one layer of aluminized mylar (0.13 mm thickness). After wrapping, each crystal was "tuned" with a Cs^{137} source such that the relative variation in light output along each crystal's major axis on

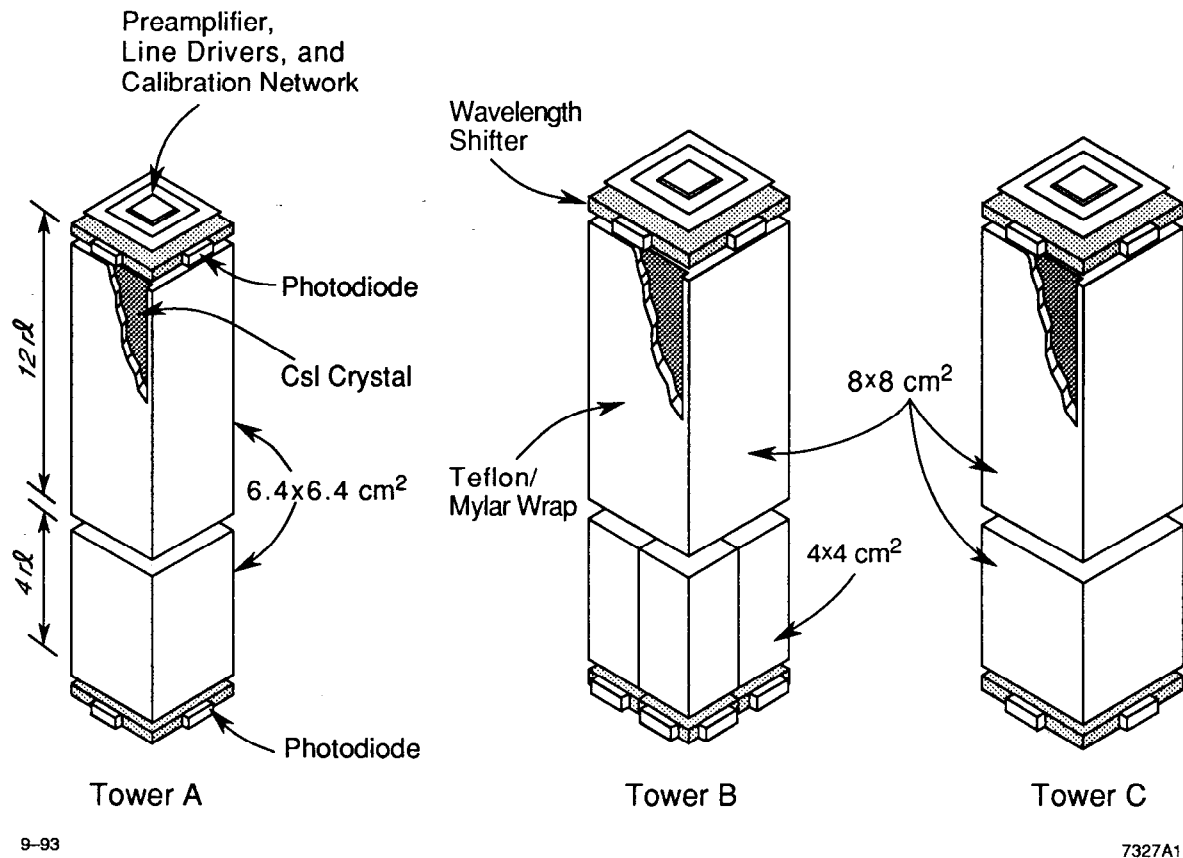
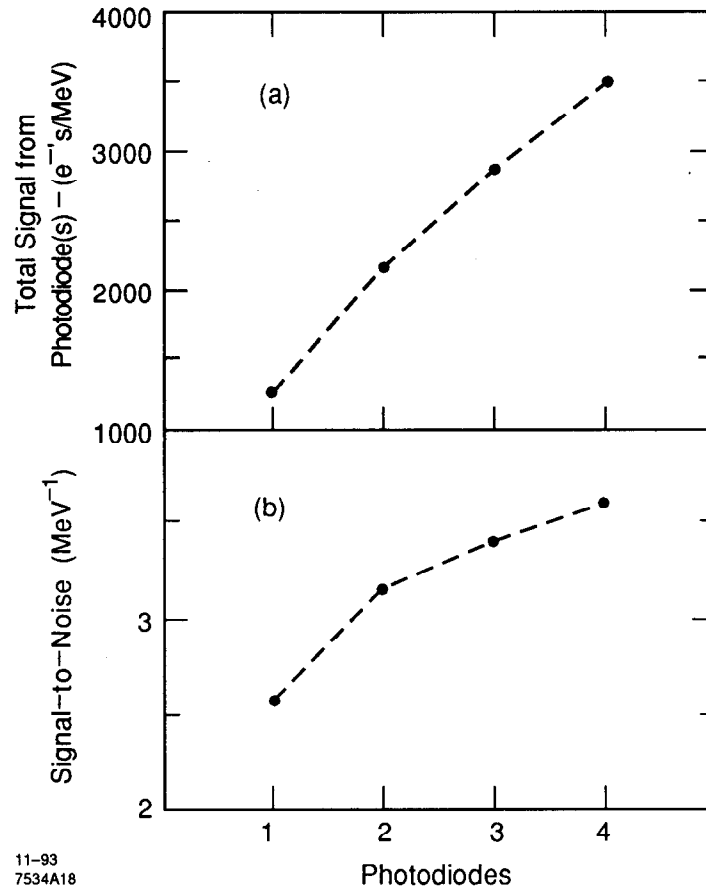


Fig. 2. Schematics of the three configurations of CsI crystal towers tested, showing longitudinal and transverse segmentation of crystals, and wavelength shifter-photodiode-preamplifier readout.

all four sides was $\leq 2\%$. Tuning involved an iterative process of polishing, selective roughening of the polished surfaces, and subsequent re-wrapping and testing of the crystals. For the short $4.0 \times 4.0 \text{ cm}^2$ crystals, we achieved about 1% nonuniformity over most of the length. One of the drawbacks of the $6.4 \times 6.4 \text{ cm}^2$ and $8 \times 8 \text{ cm}^2$ 4 rl front crystals is that their aspect ratio exhibited a larger fractional longitudinal nonuniformity near their ends. However, to compensate, the front and back crystals can be tuned together.

2.3 Wavelength Shifter and Photodiode Construction

The light collection for the readout of each crystal was accomplished using a 3 mm-thick square piece of wavelength-shifting acrylic plastic (WLS) that covered about 70% of one face of the crystal. (In a given tower, one WLS covered the front face of (each of) the front crystal(s) and one WLS covered the back face of the back crystal.) The WLS absorbs direct and internally reflected light from



11-93
7534A18

Fig. 3. a) The total signal in units of electrons/MeV of deposited energy versus the number of PD's on a wavelength shifter (one per WLS edge). b) Signal-to-noise ratio. These data were obtained using cosmic ray signals in a single, 16 rl-long crystal.

2.4 Crystal Tower Housing

The crystals within each tower and their associated electronics were isolated from neighboring crystals by enclosing them in a 0.5 mm-thick, copper-clad G-10 box. In a real detector, the box material can be reduced by using, for example, a nickel-plated, carbon-fiber epoxy laminate material. Monte Carlo studies have shown that tilting the boxes by as little as 25 mr to the incident particle direction eliminates the deleterious effects of the box's thickness on resolution. In the beam test, the boxes also served to mechanically position the front and back crystals within a tower, and to maintain a fixed WLS-to-crystal air gap.

2.5 *Overview of Readout Electronics*

The circuitry on each preamplifier board, as shown in Figs. 4-5, consisted of a FET and an ASIC-based buffer amplifier, a calibration network, and CLEO-II-style differential line-drivers [6]. Bias voltage for the PD, power, and calibration signals were also routed on the board. To reduce pickup, all PD signals were carried to the preamplifiers on 0.3 mm-diameter micro-coaxial cable of 1.5 pF/cm capacitance. The cables were placed along the inner edges of the G-10 boxes containing the crystals and preamplifier boards.

Differential signals were transmitted out of the crystal dry box on 5 m-long ribbon cables. They were received differentially by CLEO-II-style shaping amplifiers [6] (Fig. 6) which performed a single integration with shaping and peaking times of 3 μ s. Shaped signals were sampled with a \sim 200 ns gate around the peak, and digitized by LRS 2249A ADC's. There were a total of 120 readout channels. The preamplifier and shaping amplifier gains were separately preadjusted to give equal signals for a fixed charge injected at the inputs. Each calibration circuit was trimmed to produce a constant charge for a fixed input calibration pulse. The final electronic calibration was performed taking 100 repeated readings of all ADC's at 15 distinct DAC values. (The DAC values define the calibration charge, and span the energy range of interest in the beam test.) The calibration data were fit piecewise with a linear function and, to remove a small nonlinearity at the low end of the ADC range, a quadratic function.

2.6 *Preamplifier / Shaper Amplifier Description and Noise Limitations*

The desired performance for light collection and electronic readout is determined by the lowest energy photons of experimental interest. Considering the experience of other detectors in similar operating conditions, the flux and spectrum of background showers places a lower limit of about \sim 10 MeV on showers that will be useful for physics analyses. Intrinsic shower fluctuations at 10 MeV are \sim 1.2 MeV in CsI (refer to Section 3.3), suggesting that electronic noise performance should be maintained below this value in order that it not contribute significantly to the resolution for these low energy showers.

A signal from a single PD is typically small, between 1000-2000 e^- 's/MeV deposited in a large CsI(Tl) crystal. To facilitate detection of photons with energies at the 10-20 MeV level, the preamplifier's contribution to the electronic noise must be minimized. As the first amplification stage in a preamplifier, a

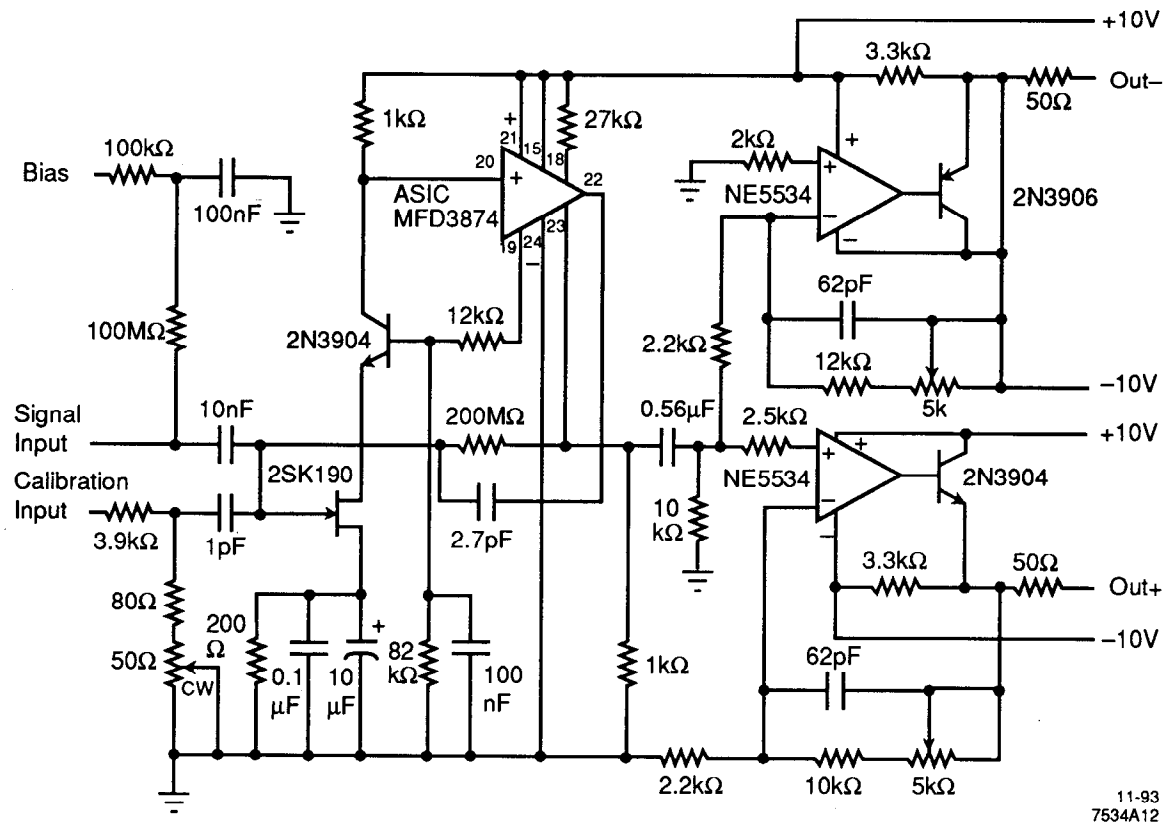


Fig. 4. Circuit diagram for the charge-sensitive preamplifier.

junction FET with high transconductance (e.g. 2SK190) gives outstanding performance. It is desirable that the rest of the system add a negligible amount of noise, such that the performance of the complete system is defined by the PIN diode shot noise, and the FET (through the capacitive load), in conjunction with the signal conditioning pulse-shaping network.

As shown in Fig. 4, the preamplifier first stage FET was followed by a semi-custom buffer amplifier (ASIC MFD3874) fabricated by Plessey (Fig. 5). Measurements were made to determine the buffer amplifier's contribution to the total noise. By placing four amplifiers on a single substrate, limits on cross talk between channels were established as <0.1%, demonstrating the possibility of dense integration on a single semi-custom chip.

The expected noise performance of the beam test electronics was calculated, including shot noise from the PD, the parallel noise from the biasing resistors, and the serial noise from the FET. When fully depleted, a PD typically has a dark current of $I_d \approx 1$ nA. Assuming a white noise spectrum,

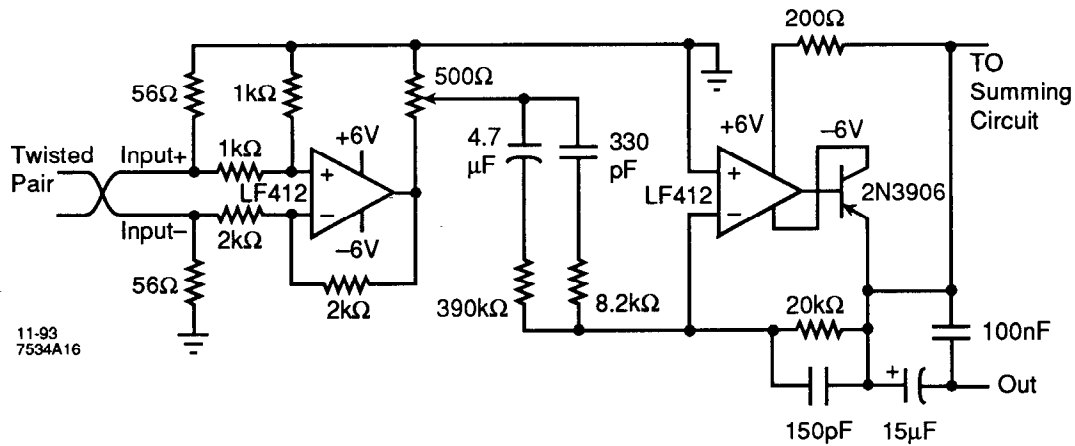


Fig. 6. CLEO II-style differential receiver and shaper amplifier.

be $410 e^-$'s. With more elaborate pulse shaping producing a sharper cutoff for the high frequency components, this result can be improved. Using a Canberra Spectroscopy Amplifier Model 2021, which provides two stages of integration with complex poles, under the same conditions, with $\tau = 4 \mu s$, an equivalent noise of $330 e^-$'s was calculated. The performance of the FET can be improved by running at current higher than the 5 mA used (increasing g_m) and with higher drain-source voltage ($> 5 V$), thereby reducing the gate capacitance. These changes increase the power consumption from 25 mW to several hundred mW, which may be unacceptable in some applications. For $g_m = 80 \text{ mS}$ and $C_g + C_d = 90 \text{ pF}$, the noise reduces to $200 e^-$'s. For low capacitive loads, a FET with lower input capacitance and correspondingly lower transconductance may give overall better results.

Measurements with the prototype charge amplifier were performed using cosmic ray signals from a $6.4 \times 6.4 \text{ cm}^2$, 12 rl long CsI(Tl) crystal. For these tests, the crystal was positioned on its side and, depending on their angle of incidence, the cosmic rays traversed about 6.4 cm of the crystal. The signals of four PD's viewing the WLS were routed to the prototype preamplifier located behind the crystal, then to the Canberra shaping amplifier and an ADC.

The average signal for a cosmic ray muon traversing the crystal was 6.3 fC/PD . Assuming 36 MeV deposited in the crystal, this results in $1100 e^-/\text{MeV}$. The noise measured for the bare amplifier was $450 e^-$'s. With the PD connected, the noise increased to $800 e^-$'s, or an energy equivalent of 0.73 MeV. Summing the signals of four PD's, a charge of 25 fC and noise equal to $1700 e^-$'s or 0.38 MeV equivalent energy were measured.

The measured noise for the bare amplifier ($450 e^-$'s) is higher than would be estimated from the previous analysis, where parallel noise from the PD biasing resistors on the preamplifier ($140 e^-$'s) and serial noise from the FET ($230 e^-$'s, with $C_i = 0$ in the absence of the PD) add in quadrature to $270 e^-$'s. This indicates that the buffer amplifier contributes to the noise and that there may be some electronic pick-up. A systematic investigation [7] showed that under conditions where pick-up was excluded, the theoretical noise for the FET alone could be achieved by a reduction in the standing currents in the buffer amplifier. Alternately, by replacing the Wilson current source used in the present design by a simpler structure or by a junction FET, a reduction in shot noise should be achievable at the larger standing currents, which may be needed to reach the required slew rates.

However, the increase (to $800 e^-$'s) after connecting the PD cannot be explained by added shot noise and capacitive load from the PD. The prediction for PD plus FET noise is $470 e^-$'s. Cabling to the PD acts as an antenna, and was observed to pick up signals generated in the lab. In the beam test, the average noise/PD was even higher (0.5-1.5 MeV) owing to poorer shielding, noise pickup, and higher leakage current caused by non-uniform cooling of the PD's and electronics within the dry-box. Integration of the FET preamplification stage with the PD may be a future option to reduce C_i and the potential for this pick-up.

3. Test Results

Results are presented for three crystal towers, each having a different geometrical configuration. As indicated in Fig. 1, Tower A refers to a contained $6.4 \times 6.4 \text{ cm}^2$ crystal tower, Tower B refers to a contained $8 \times 8 \text{ cm}^2$ crystal tower segmented into a 2×2 square array of four $4 \times 4 \text{ cm}^2$, 4 rl crystals in front and an $8 \times 8 \text{ cm}^2$ 12 rl crystal in back, and Tower C refers to an uncontained $8 \times 8 \text{ cm}^2$ crystal tower. A contained tower is one that is surrounded on all sides by other towers, so that energy shared with adjoining towers can be taken into account in determining resolutions. To determine the energy resolution and test linearity, we evaluated data taken at three beam energies for each of the three tower configurations (120, 250, and 400 MeV for Towers A and B, and 120, 200, and 400 MeV for Tower C). Position resolution was studied for Towers B and C at four beam energies (120, 200, 250, and 300 MeV).

3.1 Calibrations

After electronic calibrations have been applied, single monolithic crystal towers, such as are used in the CLEO-II and Crystal Barrel detectors, require a single overall gain constant to relate light output to energy. In contrast, the longitudinal segmentation of crystals within a tower introduces an additional calibration constant for each tower, so the beam test data for each tower were calibrated in two steps. First each PD signal on each crystal in a tower was adjusted, then a weighting constant relating the signals from the front and back crystals in a tower was determined. The calibration was performed at the highest beam energy for which data were available (≤ 400 MeV).

As the first step, the gain constant of each PD signal was adjusted so that all PD's viewing a single crystal (either front or rear) read the same average signal at the beam calibration energy. Since the beam contains e^- 's, π^- 's, and μ^- 's, this calibration can be done using either the distinct peaks of minimum-ionizing-particles or the averages of the showering-particle spectra.

The second step in the calibration involved the relative weighting of signals from PD's associated with the front and back crystals in the tower. At this stage, the following selection criteria, also used for energy and position resolution studies, were applied. A time-of-flight cut was made to select e^- 's, and minimum energy cuts were made to reject minimum ionizing particles. Additionally, to guarantee a single well-defined trajectory, using the beam-defining drift chamber, track quality cuts were made, requiring at least two hits in one dimension and at least three hits in the other dimension. A fiducial cut limiting the beam profile to 3×3 cm² was then imposed.

After applying the above criteria, to find the front-to-back (F/B) weighting constant, signals from all PD's on each crystal in a tower were summed and the average taken. As an example, the average energy spectra measured by the PD's in the back and front crystals for Tower A are shown in Figs. 7a and 7c [8], respectively [9]. The average signals from the front and back crystals in the tower were scaled separately such that on average, the sum of the front and back signals for an event is equal to the beam energy. This is illustrated in Fig. 7b [8], where the line through the x and y intercepts at the beam energy is not a fit but only to guide the eye. Finally, the spectra peak for the sum of energy in the front and back crystals in the tower was adjusted to the beam energy.

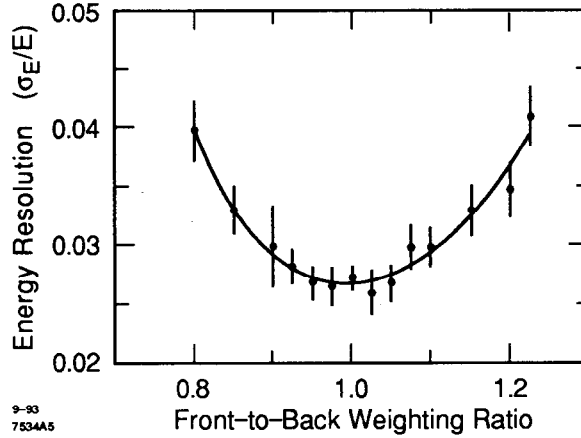


Fig. 8. Variation in σ_E/E as the relative weighting of the signals from the front and back crystals in Tower A are varied at the calibration energy of 400 MeV.

calibration beam energy. The distributions of total energy deposited at different beam energies (as shown in Fig. 9 (10) for Tower A(B)) were then fit with a Gaussian to determine the peak and the width, or σ_E/E . To define the energy resolution, we avoid the low energy radiative tails by fitting the spectra from 50% of the maximum height on the low side, to 5% of the maximum height on the high side. Systematic errors resulting from the fit were estimated by varying the endpoints and background shapes in the fit on each side of the central value.

The linearity of each tower was determined by calibrating at one beam energy, then measuring the central value of the spectra at the other beam energies. The linearity is sensitive to the front-to-back weighting, and to the lateral sharing of energy. Using this calibration procedure, as indicated by the results in Table 1, we observe that the linearity is 0.25% for Tower A and 0.35% for Tower B, where linearity is defined as the fractional error on the slope of a straight-line fit to the data points.

Results for Towers A and B at three beam energies are summarized in Table 1 and illustrated in Figs. 11a and 11b. The result of a fit to the energy resolution versus incident energy for Tower A is:

$$\frac{\sigma_E}{E} = \frac{(1.83 \pm 0.05)\%}{\sqrt{E(\text{GeV})}}$$

and for Tower B is:

$$\frac{\sigma_E}{E} = \frac{(1.69 \pm 0.08)\%}{\sqrt{E(\text{GeV})}}$$

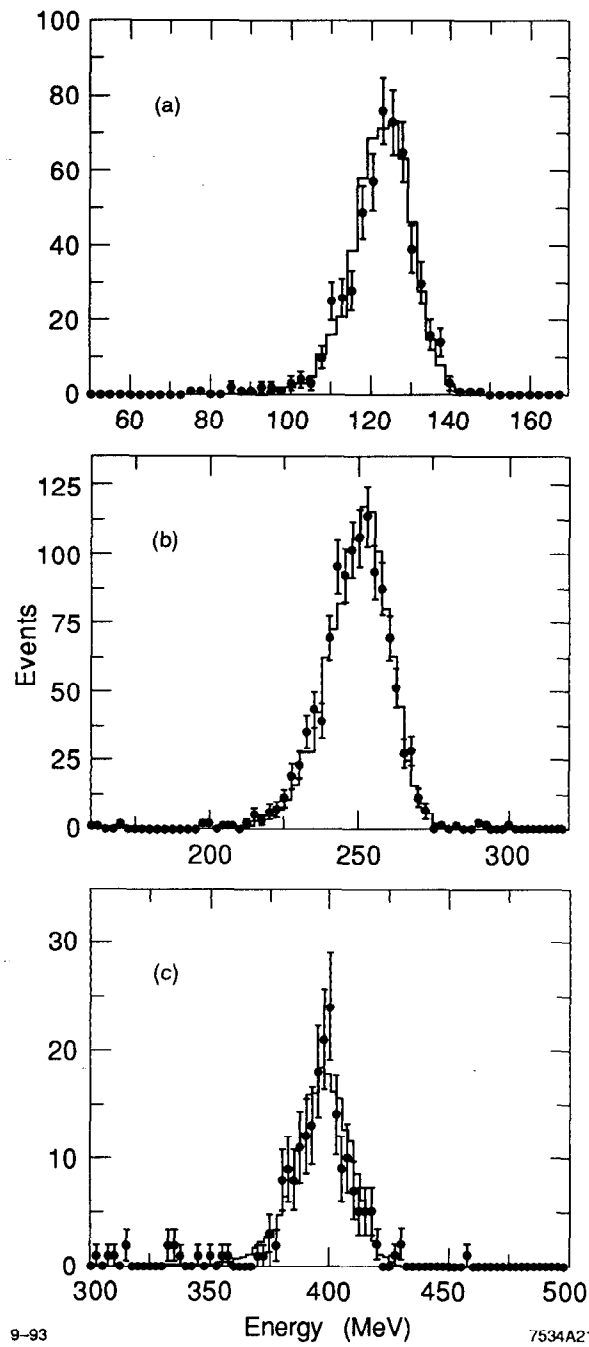


Fig. 9. Spectra of total energy, including energy shared with adjoining towers, for beam incident into center of Tower A at a) 120, b) 250, and c) 400 MeV. Data are fit to Monte Carlo (histogram) described in Sec. 3.3.

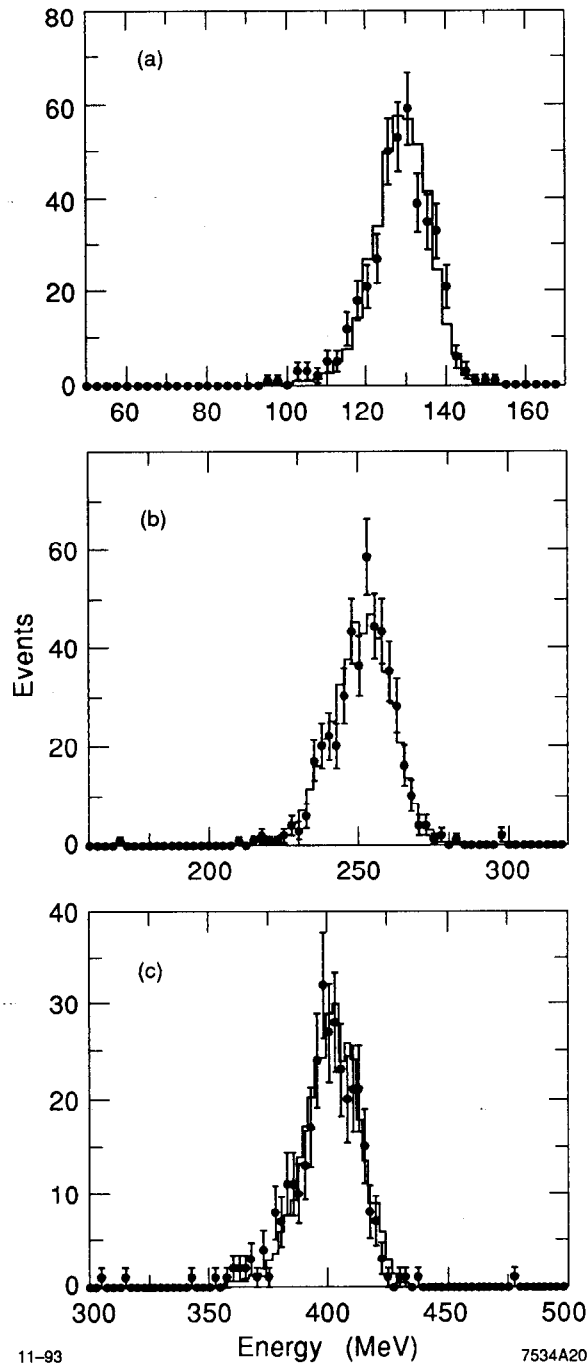


Fig. 10. Spectra of total energy, including energy shared with adjoining towers, for beam incident into center of Tower B at a) 120, b) 250, and c) 400 MeV. Data are fit to Monte Carlo (histogram) described in Sec. 3.3.

As Tower C was not fully contained, it is not included in Table 1. For completeness, and for purposes of comparison with Tower C, σ_E/E was also determined for Towers A and B in an analogous uncontained configuration, without adding in the energy deposited in adjacent towers. These results are summarized in Table 2 and Fig. 11c. The effects of non-containment on energy resolution and linearity are evident, as are changes in resolution and linearity with crystal size. Due to our fitting procedure, the differences in measured energy between the uncontained and contained configurations are only evident at the lowest energy.

Table 1. Results for contained crystal tower arrays A and B.

(*) indicates calibration energy.

Tower Size (cm ²)	Beam Energy (MeV)	Measured Energy (MeV)	σ_E (MeV)	Energy Resolution (σ_E / E)
A 6.4 x 6.4	120	124.1±0.5±0.5	6.6±0.3±0.3	0.053 ±0.003±0.003
	250	252.1±0.5 ±0.6	9.4±0.3±0.4	0.037 ±0.001±0.002
	400*	400.0±1.1±0.9	9.7±1.1±0.3	0.024 ±0.003 ±0.008
B 4-4 x 4	120	130.5±0.4±0.4	6.7±0.3±0.3	0.052±0.003± 0.002
	250	252.7±0.8±0.4	8.2±0.6±0.3	0.033±0.002±0.001
	400*	400.0±1.2±0.7	10.2±0.5±0.8	0.026±0.002±0.001

Table 2. Results for uncontained crystal tower arrays A,B, C

(*) indicates calibration energy.

Tower Size (cm ²)	Beam Energy (MeV)	Measured Energy (MeV)	σ_E (MeV)	Energy Resolution (σ_E / E)
A 6.4 x 6.4	120	112.8 ±0.6±0.8	10.4± 0.5 ±0.4	0.092 ± 0.004±0.004
	250	251.8 ±0.6± 0.8	15.6 ± 0.5 ±0.5	0.062±0.002 ±0.002
	400*	400.0±2.6±0.5	21.0 ± 2.2 ±0.5	0.052 ±0.006 ± 0.013
B 4-4 x 4	120	120.9±0.6± 0.9	7.7± 0.5 ± 0.9	0.064 ±0.004±0.007
	250	248.8±0.7±0.4	11.5± 0.5 ±0.5	0.046 ±0.002±0.002
	400*	400.0±1.4 ±1.2	13.7± 1.1 ±1.0	0.034 ±0.003±0.002
C 8 x 8	120	110.0±0.5±0.9	6.3±0.4 ±0.7	0.057 ±0.003±0.006
	200	207.4±0.5±1.1	9.2±0.4±0.7	0.044 ±0.002±0.004
	400*	400.0±1.6± 2.6	13.8± 1.2±1.9	0.034 ±0.003±0.005

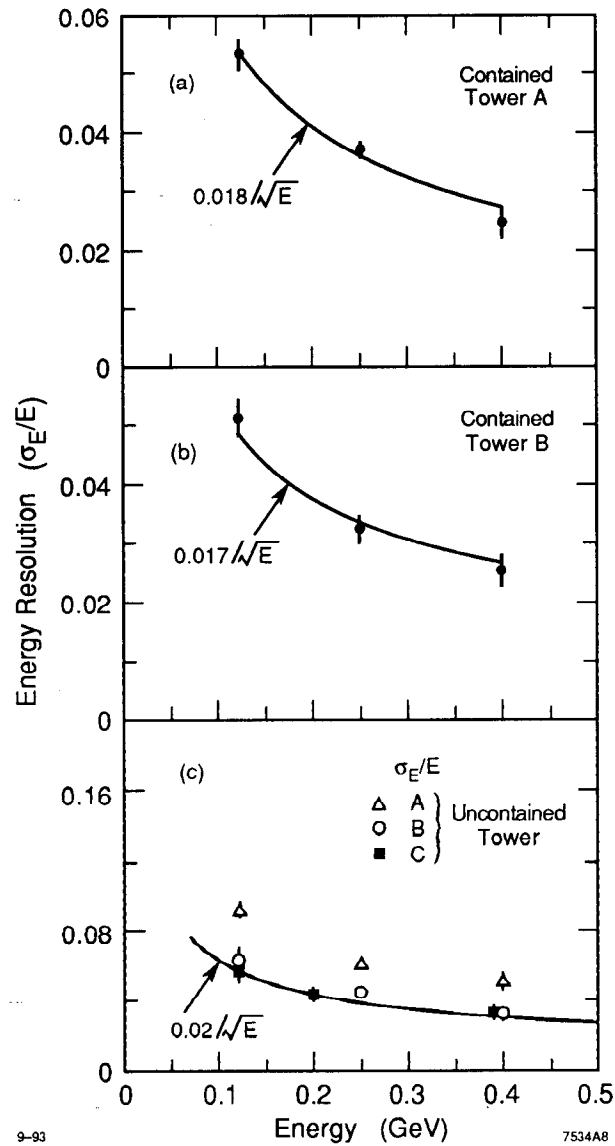


Fig. 11. a) Energy resolution for contained Towers A at 120, 250, and 400 MeV. b) Energy resolution for contained Tower B at 120, 250, and 400 MeV. c) Energy resolution for uncontained Tower C at 120, 200, and 400 MeV. For purposes of comparison only, uncontained resolution for Towers A and B is also shown.

3.3 Simulation of Energy Resolution

The Monte Carlo program EGS4 [10] was used to simulate the distribution of deposited energy for the various CsI crystal tower configurations. Fluctuations due to transverse and longitudinal shower leakage from the CsI fiducial region, and fluctuations resulting from absorption in inactive material, contribute to the energy resolution and are included in the EGS4 model. We find that for all contained tower configurations, the contributions to the resolution from these effects is small compared to the observed resolution from the beam data. In fact, the observed energy distributions are well-fit by a Gaussian term convoluted with the shower fluctuations from the EGS4 model, as shown by the comparisons to data in Figs. 9 and 10. Therefore, the resulting energy resolution is given by:

$$\left(\frac{\sigma_E}{E}\right)^2 = \left(\frac{\sigma_g}{E}\right)^2 + \left(\frac{b}{\sqrt{E}}\right)^2,$$

where b is determined by the EGS4 model of the shower, σ_g is the RMS width of the Gaussian term, and E is the incident electron energy. As discussed in Section 2.6, the Gaussian term is consistent with electronic noise, with the noise contributions of as many as 72 PD's added in quadrature for a single shower. Values of σ_g required to describe the data are in the range 5-9 MeV, depending on data run and tower configuration. The second term describes the intrinsic resolution of the CsI configurations in the low-noise limit. Using the Monte Carlo data, we find $b = 0.014 \text{ GeV}^{1/2}$ for Tower A and $b = 0.013 \text{ GeV}^{1/2}$ for Tower B. The intrinsic resolution at low energy is important for determining the required level of electronic noise. We extended the EGS4 model to low energy and found $b = 0.012 \text{ GeV}^{1/2}$ at 10 MeV beam energy for these geometries.

It is interesting to note that the energy distributions (for data and Monte Carlo) are very well modeled by the form:

$$\frac{dN(E)}{dE} = A \int_0^{E_0} e^{-\beta(E_0-E')} e^{-(E-E')^2/2\sigma_g^2} dE',$$

where A, β, E_0 , and σ_g are parameters of the fit. E_0 and σ_g represent, respectively, the beam energy and noise parameter, and hence may often be

known independently, leaving a two-parameter fit. The first term in the above equation represents energy loss by absorption or bremsstrahlung, while in our case, the second term is dominated by the electronic noise. By integration of the equation, one sees that β is related to the resolution parameter b by $1/b \approx \beta\sqrt{E_0}$.

4. Position Resolution

Above ~ 100 MeV, for crystals with transverse dimensions comparable to their Molière radius (~ 3.8 cm for CsI(Tl)), one can take advantage of the spreading of showers into neighboring crystals to accurately measure position. At very low incident energies, single Compton scattering and pair production dominate, reducing shower sharing significantly. At modest energies, a position calculation using a simple center-of-gravity (CG) method consists in taking the energy-weighted average of the central and neighboring crystals' positions using the formula:

$$CG = \frac{\sum_i E_i \cdot x_i}{\sum_i E_i},$$

where x_i is the center of crystal i , and E_i is the energy deposited in crystal i . For showers contained largely within the central crystal tower, this expression is dominated by the position of the central tower, and varies little with incident beam position until the edges of the crystal are approached, where shower sharing starts to take place. This is illustrated in Fig. 12, where the variation in the center-of-gravity (CG) position with the true beam position measured by the beam-defining drift chamber is shown. The steep slopes near the crystal edges indicate good spatial sensitivity, while the flatter slope in the middle of the crystal reflects the lack of energy sharing.

This basic CG method can be augmented to obtain improved position resolution. We calculated, for each measured CG bin, the average of the true beam positions (from the drift chamber) that contribute to the bin. This average beam position was then defined to be the "corrected" CG value for the measured CG value. This technique gives an improved position estimate, as shown in Fig. 13, and is based on a mathematically equivalent technique used by CLEO [6]. The position resolution is defined as the difference between the true incident position measured by the drift chamber and the position reconstructed from the

crystal CG with these average corrections applied. The position resolutions we quote were obtained by fitting these residuals to a Gaussian function.

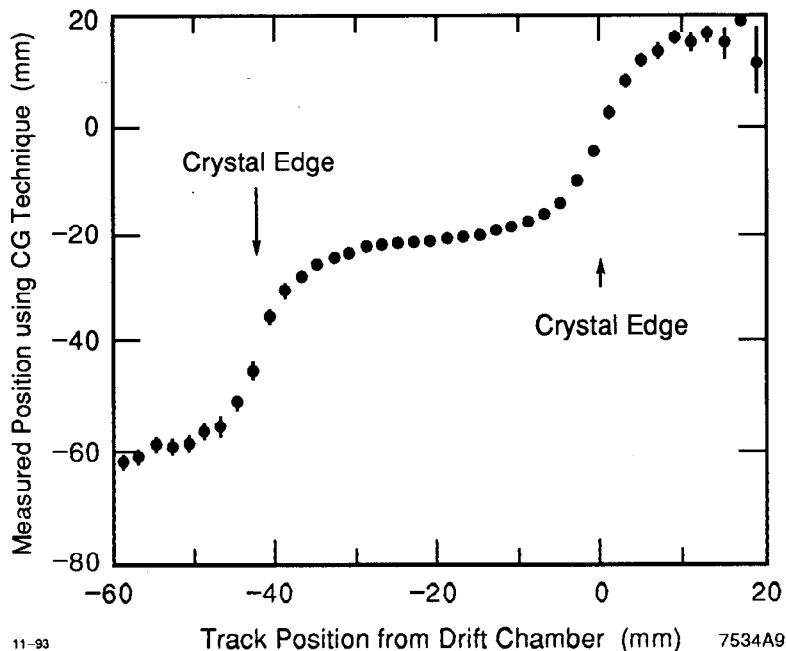


Fig. 12. Average center-of-gravity position as a function of true track position.

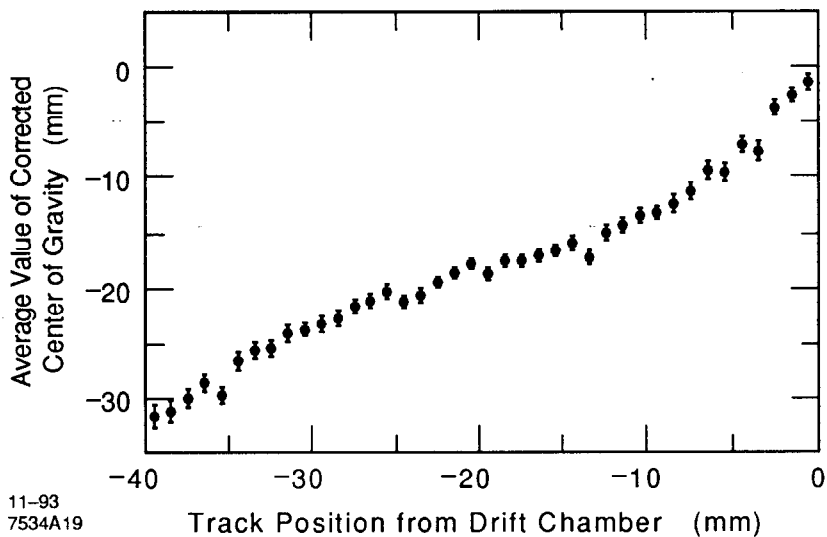


Fig. 13. Average corrected center of gravity as a function of track position.

Position resolution was determined for Towers B and C only. Insufficient data were accumulated to evaluate the resolution over the full face of Tower A. Resolutions were determined using e^- 's, with the same time-of-flight and energy

deposition cuts as were used for energy resolution studies. Position resolution for Tower C was calculated using the energy deposited in the front and back crystals in the tower. Since Tower C was illuminated only on one side, the resolution plot was folded across the center [11]. This introduces a systematic error the size of which can be estimated by studying the effects of the same folding on Tower B. The position resolution for Tower B was determined using the four 4-rl-thick front crystals only, to take advantage of their smaller lateral dimensions.

To evaluate the average position resolution in a crystal, a subset of all tracks in each tower was chosen to enforce a uniform illumination across its face. An example of the Gaussian fit at 200 MeV for Tower B is shown in Fig. 14. The average position resolution results are summarized in Table 3. The position resolution varies slowly with energy over the range we studied, and can be parameterized in the form:

$$\sigma_x = a + \frac{b}{\sqrt{E}}.$$

Fits to this form are shown in Fig. 15, and the fit parameters (a,b) for each Tower are given in Table 4.

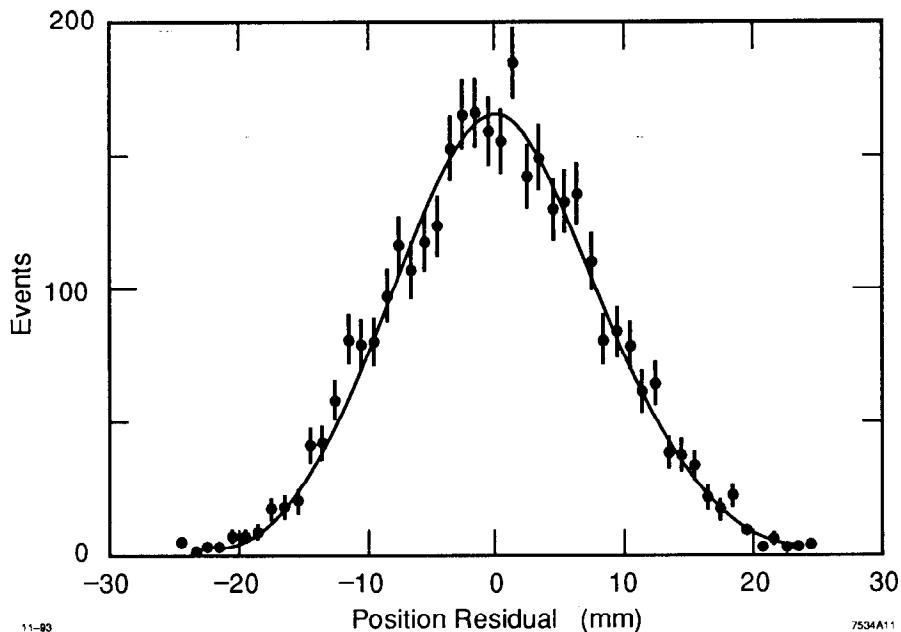


Fig. 14. Residual of average position over the face of Tower B at 200 MeV, with Gaussian fit superimposed.

Table 3. Average position resolution over faces of Towers B ($4 \times 4 \text{ cm}^2$) and C ($8 \times 8 \text{ cm}^2$). Statistical errors are given first. See note in text regarding Tower C systematic errors.

Beam Energy (MeV)	Tower B Resolution (mm)	Tower C Resolution (mm)
120	9.1 ± 0.1	$15.1 \pm 0.1 \pm 0.7$
200	8.0 ± 0.1	$11.8 \pm 0.1 \pm 0.4$
250	7.0 ± 0.1	$11.9 \pm 0.1 \pm 0.4$
300	6.5 ± 0.2	$11.9 \pm 0.2 \pm 0.6$

Table 4. Average position resolution results for the fit: $\sigma_x = a + \frac{b}{\sqrt{E}}$.

Tower	a (mm)	b (mm-GeV ^{1/2})
Tower B	2.5 ± 0.9	2.3 ± 0.4
Tower C	5.8 ± 2.8	3.0 ± 1.5

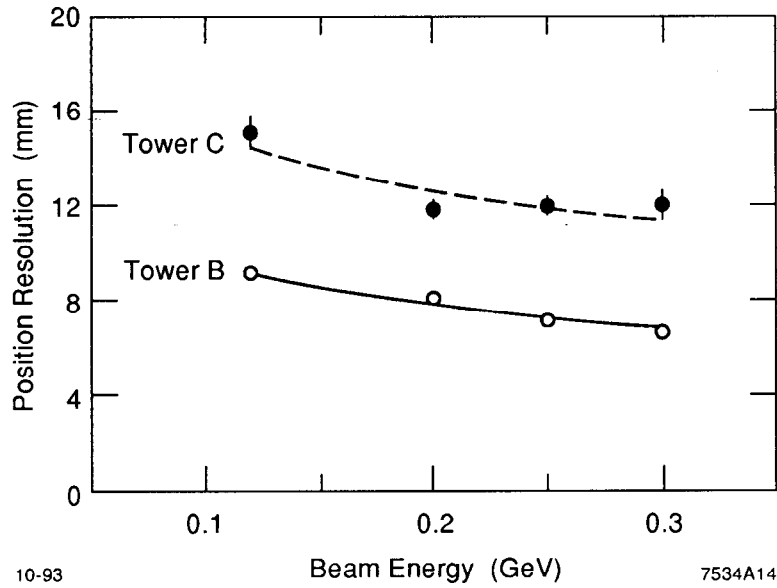


Fig. 15. Position resolution for the front $4 \times 4 \text{ cm}^2$ crystals in Tower B and for the front and back crystals in Tower C, each fit with the form $a + b/\sqrt{E}$, where a and b are given in Table 4.

5. Conclusions

We have presented results on energy resolution and linearity, and position resolution, for specific crystal tower configurations in an array of longitudinally-segmented CsI(Tl) crystals, where each crystal is readout with a wavelength shifter and from two to four photodiodes. These measurements demonstrate that linearity and energy resolution are preserved in the presence of a longitudinal division near shower maximum, and additional transverse division of the front section, of the crystals. Crystal segmentation can be easily achieved with PD/WLS readout techniques. The segmentation of crystals within the towers can provide additional information on particle identification, range, and direction. This additional information may be necessary for background rejection in high luminosity e^+e^- and hadron colliders.

When energy shared with adjoining towers is taken into account, the energy resolution achieved appears independent of the type of tower configuration. We find an energy resolution consistent with $(1.83 \pm 0.05)\% / \sqrt{E(\text{GeV})}$ for Tower A and $(1.69 \pm 0.08)\% / \sqrt{E(\text{GeV})}$ for Tower B. The EGS4-based simulation indicates that the energy resolution measured in our data is well-described by an intrinsic shower fluctuation term (b/\sqrt{E}) added in quadrature with a Gaussian term consistent with electronic noise (σ_g/E). We find $b = 0.013 \text{ GeV}^{1/2}$ and $b = 0.014 \text{ GeV}^{1/2}$ for Towers A and B, respectively. The position resolution improves with finer crystal segmentation and can be parameterized as $a + b/\sqrt{E}$, where $(a,b) = (2.5 \pm 0.9 \text{ mm}, 2.3 \pm 0.4 \text{ mm-GeV}^{1/2})$ for Tower B and $(a,b) = (5.8 \pm 2.8 \text{ mm}, 3.0 \pm 1.5 \text{ mm-GeV}^{1/2})$ for Tower C.

Acknowledgments

For their gracious assistance during the beam test of our CsI crystal array at TRIUMF, we thank the TRIUMF physicists and staff, particularly D. Ottewell and D. Diel. One of us (A.D.F.) would like to thank the University of Illinois Campus Honors Program for support.

References

1. See for example, R. H. Schindler, *Proceedings of the Tau-Charm Factory Workshop*, SLAC, Ed. L. Beers, SLAC REPORT-343 (1989) 127.
2. D. Stoker, *Proceedings of the Tau-Charm Factory Workshop*, Universidad de Sevilla, Andalucia, Spain (May 1991).
3. R. Schindler, in *Proceedings of the Tau-Charm Factory Workshop*, Universidad de Sevilla, Andalucia, Spain (May 1991).
4. TRIUMF Users Handbook, IV-11 to IV-15, (1987).
5. Crystal Barrel Collaboration (E. Aker, *et al.*), NIM A 321, 69 (1992).
6. E. Blucher, *et al.*, Test of Cesium Iodide Crystals for an Electromagnetic Calorimeter. NIM A 249, 201 (1986).
7. D. R. Freytag and G. M. Haller, SLAC-PUB-6351 (September 1993) (to be submitted to *Nuclear Instruments & Methods*).
8. The minimum ionizing signal seen in Figs. 7b-7c is removed by the selection criteria described previously in this section. It is plotted here only to allow comparison of the minimum ionizing and showering particle signals.
9. Tower A was calibrated using data taken at 400 MeV. Data taken at 250 MeV is shown in Fig. 7 because the relative abundances of minimum ionizing and showering particles available at this energy better illustrates the particle separation attainable with longitudinally-segmented crystals.
10. W.R. Nelson, H. Hirayama, and W.O. Rogers, SLAC-Report-265 (1985).
11. Only half of Tower C was illuminated. Therefore, to evaluate the position resolution of Tower C, Tower B (which adjoins Tower C) was taken to be the center and, in addition to Tower C, the crystal tower on the opposite side of Tower B was also used. This technique assumes that the position resolution is symmetrical, so a systematic error is introduced to take into account the fact that the resolution may not be centered.